Estimating joint contact areas and ligament lengths from bone kinematics and surfaces

Georgeta Elisabeta Marai, David H. Laidlaw, Çağatay Demiralp,
Stuart Andrews, Cindy M. Grimm, Joseph John Crisco

This work was supported in part by NSF CCR0093238 and by NIH AR44005.*Asterisk indicates corresponding author.*

*G. Marai, D. Laidlaw, C. Demiralp, and S. Andrews are at the Department of Computer Science, Brown University, Providence, RI 02912. E-mail: gem@cs.brown.edu.

C. Grimm is at the Department of Computer Science , Washington University, St. Louis, MO 63130.

J. Crisco is with the Department of Orthopaedics and the Division of Engineering, Brown Medical School/Rhode Island Hospital, Providence, RI 02912.

Abstract

We present a novel method for modeling contact areas and ligament lengths in articulations. Our approach uses volume images generated by computed tomography and allows the **in vivo** and non-invasive study of articulations. In our method bones are modeled both implicitly (scalar distance fields) and parametrically (manifold surfaces). Using this double representation we compute inter-bone distances and joint contact areas. Using the same types of representation we model ligament paths; in our model the ligaments are approximated by shortest paths in a 3D space with bone obstacles. We demonstrate the method by applying our contact area and ligament model to the distal radioulnar joints of a volunteer diagnosed with malunited distal radius fracture in one forearm. Our approach highlights focal changes in the articulation at the distal radioulnar joint (location and area of bone contact) and potential soft-tissue constraints (increased 'length' of the distal ligaments and ligament-bone impingement in the injured forearms). Results suggest that the method could be useful in the study of normal and injured anatomy and kinematics of complex joints.

Keywords

Joints, contact areas, ligament paths, differential geometry, distance fields, computed tomography.

I. Introduction

We propose a method for modeling bony contact areas and ligament paths in articulations. Contact areas define the cortical surface where bones articulate with each other. Modifications in bony contact areas and ligaments correlate with numerous joint-related post-trauma disabilities and various degenerative diseases, yet little information about the nature of these modifications is currently available. Most articulation and soft tissue studies are performed either *in vitro* or during clinical interventions, and thus reveal little information on potential modifications of soft tissue biomechanics due to injury or disease. *In vitro* specimens illustrating a specific trauma or disease are rarely available; invasive studies alter inevitably joint kinematics and thus introduce false modifications. Although *in vivo* 3-D techniques for studying the structure and kinematics of joint were recently introduced [1], [2], [3], [4], they do not attempt to capture more subtle details such as potential soft-tissue constraints or modifications in articulation. Our method successfully identifies and highlights *in vivo* and non-invasively potential focal changes and soft-tissue constraints in articulations.

In our approach, the structure and kinematics of an articulation are determined from segmented CT volume images. Bones in the joint are modeled further both implicitly, as *scalar distance fields*, and parametrically, as *manifold surfaces*. These two types of representation have complementary strengths for different types of calculations. Manifold surfaces provide an accurate, smooth, and locally controllable representation of the bones [5]. Distance fields on the other hand, have important advantages for geometric computations such as fast distance calculation, collision detection, and inside-outside tests [7]. Distance fields computed from the parametric representation provide the support for calculating contact areas. Once contact areas are calculated, focal changes in the articulation are evaluated by comparing the area and location of the bony contact.

We assess potential soft-tissue constraints by calculating the minimum 'length' of ligaments as a function of bone kinematics. Ligament paths are also modeled based on the distance field representation. We model ligaments as shortest paths between ligament insertion points – the points at which a ligament is anchored to bones; these paths are constrained to avoid bone penetration. Our model takes into account the known trajectory of a ligament and the ligament fiber orientation, the location of the ligament insertion points, and the locations of adjacent bones. The ligament model reported here is based solely on joint geometry.

We demonstrate our method by applying it to data collected from both forearms of a volunteer diagnosed with a malunited distal radius fracture in one forearm. The distal radioulnar joint (DRUJ), a complex joint involved in forearm rotation, comprises the two forearm bones (radius and ulna – Fig. 1) and a number of ligament and cartilaginous complexes. Forearm injuries involving the DRUJ often result in a significantly decreased range of rotational motion, decreased grip strength, and loss of wrist motion. The symptoms can be disabling, especially in physically active individuals or when the pathology affects a work-related activity.

Altered soft tissues and focal changes in the DRUJ articulation may be responsible for the abnormal functioning of the forearm in the absence of evident bone damage, as a recent study suggests [8]. We show that our contact-area and ligament-length model gives unexpected insight into the biomechanics of the forearm and, more importantly,

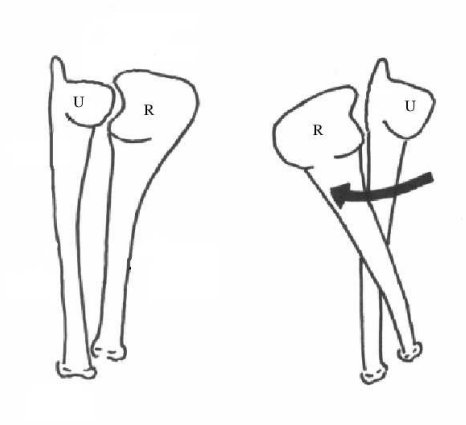

Fig. 1. The DRUJ comprises the two forearm bones – radius (R) and ulna (U). The wrist is at the upper extremity of the drawing. During forearm rotation the DRUJ goes from supination (left) to pronation (right).

reveals significant differences between uninjured and injured articulations at the DRUJ. The present study attempts to model, *in vivo* and non-invasively, potential soft-tissue constraints and focal modifications in articulations. Results indicate that our method could be useful in the study of the normal anatomy and kinematics of complex joints like the wrist and may also have applications to the study of other joints like the knee or the elbow.

II. Materials and Methods

Figure 2 depicts our method pipeline. In the first phase, image volumes of the wrists in multiple poses are acquired with a CT scanner (section II.A). From these images bones are manually segmented and further modeled as distance fields and manifold surfaces (section II.B). Kinematic information is recovered via surface registration of the bones (section II.C). Bony contact areas and ligament paths are computed using both bone representations (sections II.D and II.E). We repeat the contact-area and minimum-path computation over all joint poses for a given volunteer. Finally, contact areas and ligaments of the injured and uninjured forearm of the volunteer are compared (section II.F).

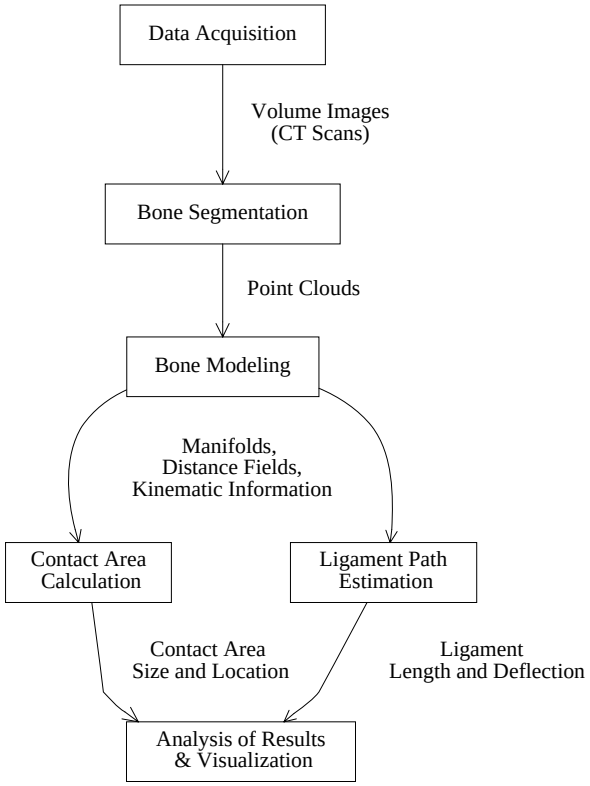

Fig. 2. Method pipeline for measurement of contact areas and ligament paths in joints. Point clouds corresponding to bone surfaces are segmented from CT volume images. Bones are further modeled as both distance fields and manifold surfaces. From the ligament-path and contact-area models we extract information characterizing the articulation that is further analyzed and presented to the user.

A. Data Acquisition

CT volume images of both wrists were obtained simultaneously with a GE HiSpeed Advantage CT scanner. Scout and reference scans were performed with the forearm and wrist in the neutral position. Additional scans were performed with the forearm at 30, 60, and 90 degrees of both pronation (i.e., forearm with the palm facing downwards) and supination (i.e., forearm with the palm facing upwards). In the forearm with limited mobility (decreased range of pronosupination), scans were made at 30 degree intervals (above), and then at the maximum rotation that could be comfortably achieved. Approximately 45 1.0 mm CT slices were acquired at each position.

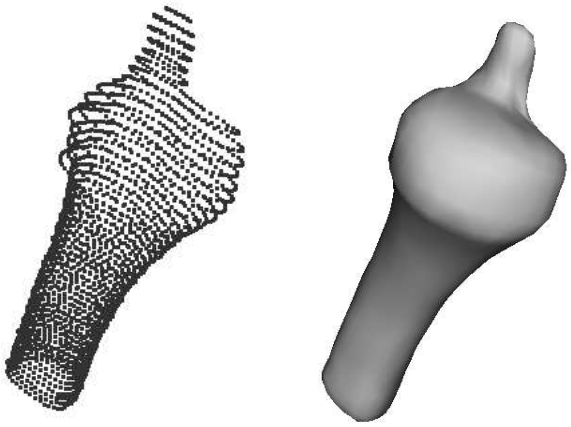

Fig. 3. Manifold surface representation of bones. Left: segmented point cloud corresponding to the ulna. Right: parametric (manifold) model of the same bone.

B. Bone Segmentation and Modeling

Points corresponding to the outer bone cortex were manually segmented from each CT slice and grouped to form a separate 3D point cloud for each bone. We reconstruct a bone surface by fitting a manifold surface to the corresponding cloud of 3D points [5] (Fig. 3); the result is a smooth, locally parameterized, C^2 continuous surface. The overlapped structure of the manifold-surface representation, which is essentially inspired by differential geometry, has several advantages including flexibility in shape adjustments without costly constraints, and smooth transitions and uniformity among patches.

The manifold model addresses difficulties introduced by the CT scanning process, such as dense sampling along sparse contours and noise [5]. The manifold model is analytic and can therefore by sampled at any resolution to produce smooth distance maps. High-resolution smooth distance maps are necessary in order to build ligament paths, as discussed in Section II.E.

By convention, we reflect left forearm data in order to directly compare it with right forearm data. The mirroring operation is purely mathematical and does not affect the data; it merely allows easier comparisons.

Modeling contact areas and ligament paths requires bone-to-bone distance information (sections II.D and II.E). The manifold surfaces provide accurate, smooth but computa-

tionally expensive distance information. We combine the manifold representation with interpolated distance fields, which are slightly less accurate but more intuitive and much faster.

Distance fields for each bone are computed using the reconstructed manifold bone models. A distance field is a scalar field that specifies the signed distance from a point to the bone surface (Fig. 4). Numerical sign is used to distinguish the inside from the outside of the bone: negative values are inside the bone, positive values are outside the bone, zero values are on the bone surface.

The distance field is computed from the manifold representation as follows: given a point P in space, the closest point Q on the manifold has the property that the surface normal at Q points in the direction P-Q. We find an approximate guess for the point Q by finding the closest point Q on the manifold mesh, then perform a gradient descent to find the Q that meets the above criteria. The inside-outside test simply involves counting the number of intersections with the manifold mesh of any ray from P [6].

In order to increase the speed of lookup operations, the distance fields are sampled on a regular grid. We use interpolation of the values at grid points to approximate the shape of the bone more accurately. The scalar field is stored as a sampled data set over a cuboid surrounding the bone. We call the result a *distance cuboid*.

The double bone representation – manifold surfaces and distance cuboids – enables us to perform further joint-related computations, such as calculation of bony contact areas (section II.D) and estimation of ligament paths (section II.E).

C. Recovery of Bone Kinematics

Recovering the bone kinematics enables us to analyze our contact area and ligament measurements as functions of wrist motion. Motion of the radius with respect to the ulna was determined for each scanned wrist rotation position. First the ulna bone was registered with respect to its neutral position to account for global changes in forearm positioning. Next, the relative motion of the radius with respect to the ulna was calculated. Registration is accomplished via a surface-distance-minimization algorithm [8].

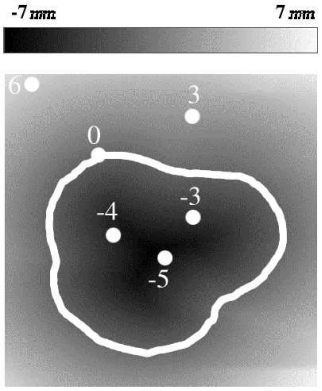

Fig. 4. Distance field representation of bones: horizontal 2D section through a signed distance field (ulna). The contour corresponds to the boundary of the bone. Sign distinguishes the inside from the outside of the bone: negative values are inside the bone, positive values are outside the bone, zero values are on the bone surface. The dark area is the inside of the bone.

D. Contact Area Calculation

The bony contact area is defined as the cortical surface area on the bone that is less than a prescribed threshold distance (typically 5 mm) from the cortical surface of a neighboring bone. Estimating contact areas requires computation of inter-bone distances within the joint.

Once distance cuboids are generated, we calculate the distance from an arbitrary point, p, and a bone surface, b, as follows. Each bone surface has a surrounding distance cuboid f_b, over which the distance field is sampled. We use tricubic B-spline interpolation to interpolate the sample values between grid locations.

The point p can be inside or outside the distance cuboid f_b. We make sure that areas of interest (i.e., articulated surfaces) are well within the distance cuboid. Figure 5 illustrates the procedure. We evaluate two cases to find the distance:

p **is inside** f_b**:** we look up f_b for p

p **is outside** f_b**:** we first find the distance to the nearest point p' on the boundary of f_b. We then add it to the distance value acquired by looking up f_b for p'

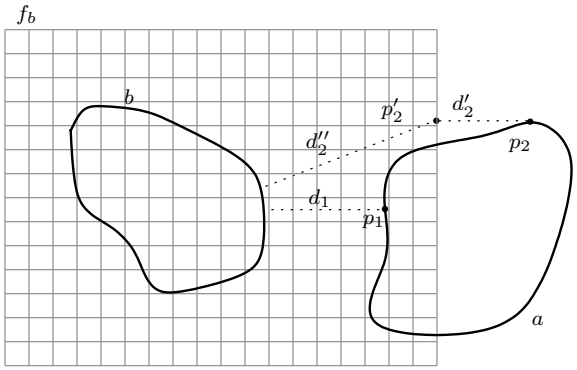

Fig. 5. 2D illustration for obtaining distances from points p_1 and p_2 to bone b. f_b is the distance cuboid for bone b. Shortest distance values to bone b at the grid intersections are known. We use tricubic interpolation for values within the grid. Since p_1 is inside the cuboid, the distance from p_1 to b is equal to $f_b(p_1) = d_1$. For p_2, we first find the distance to the closest point p_2' in the distance cuboid and then the distance between p_2 and b is approximated as $d_2' + f_b(p_2') = d_2' + d_2''$.

With this procedure we find distances from every vertex in the surface model of one bone to neighbors of interest.

Using the inter-bone distance we compute isocontours on the contact area, each contour showing where the distance map is equal to a constant distance. For efficient computation, we assume that the distance map is linear over the triangular faces that comprise the surface of the bone and thus the equal distance contours are straight line segments over each triangle. If the distance value of a contour is within the range of the distance values at the vertices, a contour line segment is generated over the triangle.

Figure 6 shows typical contact areas in the DRUJ; the joint was exploded to show the articulated surfaces more clearly. The color on bone surfaces codifies the distance to the nearest point on the opposite bone; darker regions are closer.

We characterize the contact area by its size and by the location of its centroid. The size is the area of the surface triangles within the 5 mm contour. The location of the centroid is described in cylindrical coordinates with respect to a standard coordinate system with the origin at the ulnar-carpal surface and positive x-axis in a proximal direction (Fig. 7).

It is important to note that the articular contact calculated here is an estimate of joint contact based upon the distance between cortical bone surfaces. Cartilage thickness, bone and cartilage deformation and stresses in the tissues were not considered in this study.

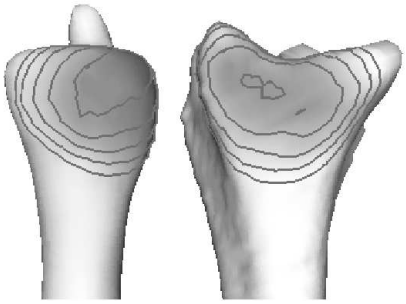

Fig. 6. Contact areas in the DRUJ. Bones are color-mapped and contoured. The color saturation on bone surfaces indicates the distance to the nearest point on the opposite bone; darker regions are closer. The joint is exploded to show the articulated surfaces more clearly. The maximum distance visualized is 5 mm; contour lines are drawn at 1 mm intervals.

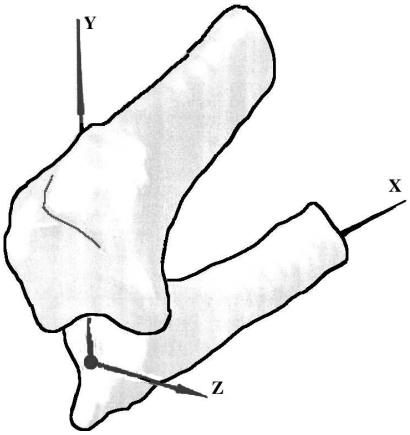

Fig. 7. Anatomic coordinate system defined on the ulna. The location and orientation of the x-axis were generated from the diaphysical cross-section centroids of the ulna, while the z-axis was defined to be perpendicular to a plane that passed through the x-axis and the tip of the ulnar styloid. The y-axis was constructed perpendicular to both the$x$- and z-axes.

E. Ligament Path Estimation

We can also use the double bone representation to construct ligament paths. We manually identify the insertion points (the points where the ligament is anchored to the bone) of a given ligament on the bone surface by using anatomical landmarks. We generate plausible ligament paths as shortest paths between insertion points, constrained to avoid bone penetration. While the paths we generate are not actual ligament paths, they give a useful lower bound on the length of these ligaments and thus help identify potential

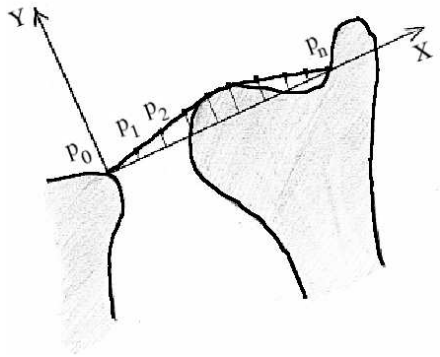

Fig. 8. Shortest path between two points p_0 and p_n (2D case); the path must not penetrate the 2D obstacle on the right. Following the optimization approach, the points p_1 to $p_n - 1$, initially equally distributed on the p_0p_n segment, increase their y coordinate so that the nonpenetration constraint is satisfied.

joint mobility constraints imposed by ligaments. In the distal radioulnar ligament case, the anatomical trajectory appears to fit the shortest-path description.

We build shortest paths via an optimization approach that exploits the distance field representation of the bones. Unlike other possible minimum-path approaches, this technique deals effectively with a large number of bone model vertices without requiring expensive restructuring – in terms of memory and time – of the search space. The resulted paths are also more accurate than those generated, for example, by graph approximation algorithms, as the method allows a large number of path control points and recovers gracefully from obstacle penetration. We begin the description of the algorithm with a simplified 2D example, shown in Fig. 8. Here we are required to find a shortest path between two points p_0 and p_n that does not penetrate the 2D obstacle on the right.

We start by attaching a local 2D coordinate system to the obstacle, so that the origin of the system is at p_0 and the x axis is the line defined by p_0 and p_n. We consider $n - 1$ points in addition to p_0 and p_n, equally spaced on the p_0p_n segment. We reformulate our problem in the following terms: "Find the coordinates of the $n - 1$ points so that the length of the path $p_0p_1p_2...p_n$ is minimum and the height of each point with respect to the obstacle surface is nonnegative." If we fix the x coordinates of the points so that they are initially equally spaced on the p_0p_n segment, our problem amounts to minimizing the

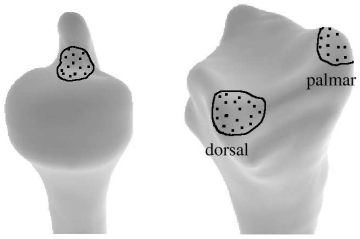

Fig. 9. Insertion point location: insertion points are chosen manually, based on anatomical information. Points are randomly distributed on the surface of the bones within a circular area with a diameter of 4 mm. Left: insertion site on the ulna. Right: dorsal and palmar insertion sites on the radius.

Euclidean length of the path over the y_i coordinates of the points:

$$\text{argmin}_{\text{y}_\text{i}} \Sigma_{i=0}^{n-1} \sqrt{(x_{i+1} - x_i)^2 + (y_{i+1} - y_i)^2} = \text{argmin}_{\text{y}_\text{i}} \Sigma_{i=0}^{n-1} \sqrt{\text{const} + (y_{i+1} - y_i)^2}$$

subject to $f_b(x_i, y_i) > 0$, $i = 0..n-1$
where $x_{i+1} - x_i = \text{const}$, $i = 0..n-1$

The formulation described above extends to 3D, where we optimize over both the y and z coordinates of the points:

$$\text{argmin}_{\text{y}_\text{i},\text{z}_\text{i}} \Sigma_{i=0}^{n-1} \sqrt{\text{const} + (y_{i+1} - y_i)^2 + (z_{i+1} - z_i)^2}$$

subject to $f_b(x_i, y_i, z_i) > 0$, $i = 0 : n-1$

The extension of the algorithm to any number of obstacles is straightforward.

We use a sequential quadratic programming method [9] to solve the optimization problem. The sequential quadratic programming method is fast and robust and handles both nonlinear objective functions and nonlinear constraints. Although it is a general concern that nonlinear optimizations can become trapped in suboptimal local solutions, in our experience this has not been a problem. We have found that additional iterations of the optimization process with significantly different start positions converge to the same solu-

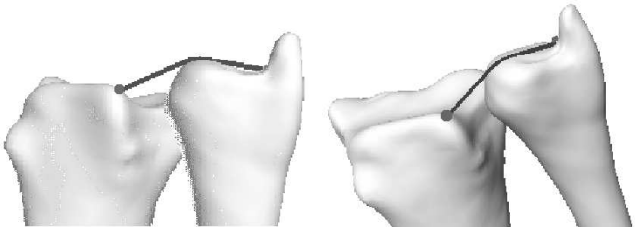

Fig. 10. Shortest paths (dark gray lines) generated by the ligament model.

tion. We are currently using three different start solutions:

1. points on the straight p_0p_n line;
2. points on a randomly displaced path;
3. points generated by the procedure in the previous pronosupination position.

The optimization procedure converges to the same solution in all three cases. This outcome is justified by the smooth structure and fine resolution of the search space generated by the distance field representation.

We tried several values for the number of points n. In the DRUJ case, as n approaches 40 the total length of the path converges to a stable value. For this value of n the length of each mini-segment in the path drops below 0.2 mm, which provides sufficient accuracy to detect deflection of the ligament by the bone. Figure 10 shows two shortest paths generated with our algorithm.

We considered several plausible insertion points for each ligament, as precise information on insertion point location was not available. The insertion points were generated by randomly distributing points around a manually chosen landmark on the surface of the bones, within a circular area with a diameter of 4 mm (Fig. 9). The insertions were defined on the ulna at the base of the styloid for both ligaments and on the radius at the dorsal and palmar prominences of the sigmoid notch, respectively. The locations of the insertion sites and the area of insertion were derived from anatomical descriptions in the literature [32], [33], [34], [35]. The results of the insertion point study are presented in section III.

We characterize the ligament paths by their lengths and their 'deflection'. Lengths are normalized with respect to the uninjured length in neutral pronosupination. Deflection is

defined as the maximum distance across all path points to the straight line defined by the two ligament insertion points.

The ligament-length model reported here is based solely on joint geometry. Structural and material properties of the ligaments were not taken into account in this study.

F. Visualization and Analysis of Results

The software package we have developed for visualizing the results of our technique consists of C++ and Open Inventor code and runs on the SUN UltraSparc and Windows platforms.

We visualize contact areas using color mapping and contouring. Color maps are generated for each bone so that distance values of surface points are mapped to varying color saturations (more saturated colors represent shorter distances). Distances larger than the contact threshold value (5 mm) are neither colored nor contoured and are shown as white surfaces. Contours and ligament paths are visualized as polylines.

We also analyze the results quantitatively by comparing ligament length, ligament deflection, contact area size, and contact area centroid location between the injured – malunited distal radius fracture – and uninjured forearm of the same volunteer.

III. Results and Discussion

Generating contact areas over different forearm rotation positions yields sequences like those in Fig. 11. The decreased size and shifted location of the bony contact area in the injured case is noticeable, especially towards pronation.

Figure 12 quantifies the size of the ulnar contact area at a threshold of 5 mm for the volunteer's uninjured and injured forearm. For the uninjured wrist, contact area was positive for a 3 mm threshold as well. For the injured wrist, there were several poses, mostly pronated, in which the 3 mm contact area was absent. Together with the 5 mm contact area changes, this suggests an increased gap between the bones in the injured case.

We measured contact area as a region on the ulnar surface close to the radius; an analogous measure on the surface of the radius can also be defined. We found that the area measure was somewhat larger (10-20%), but followed the same trends as the ulnar contact area. The size difference is consistent with the concave contact area on the radius,

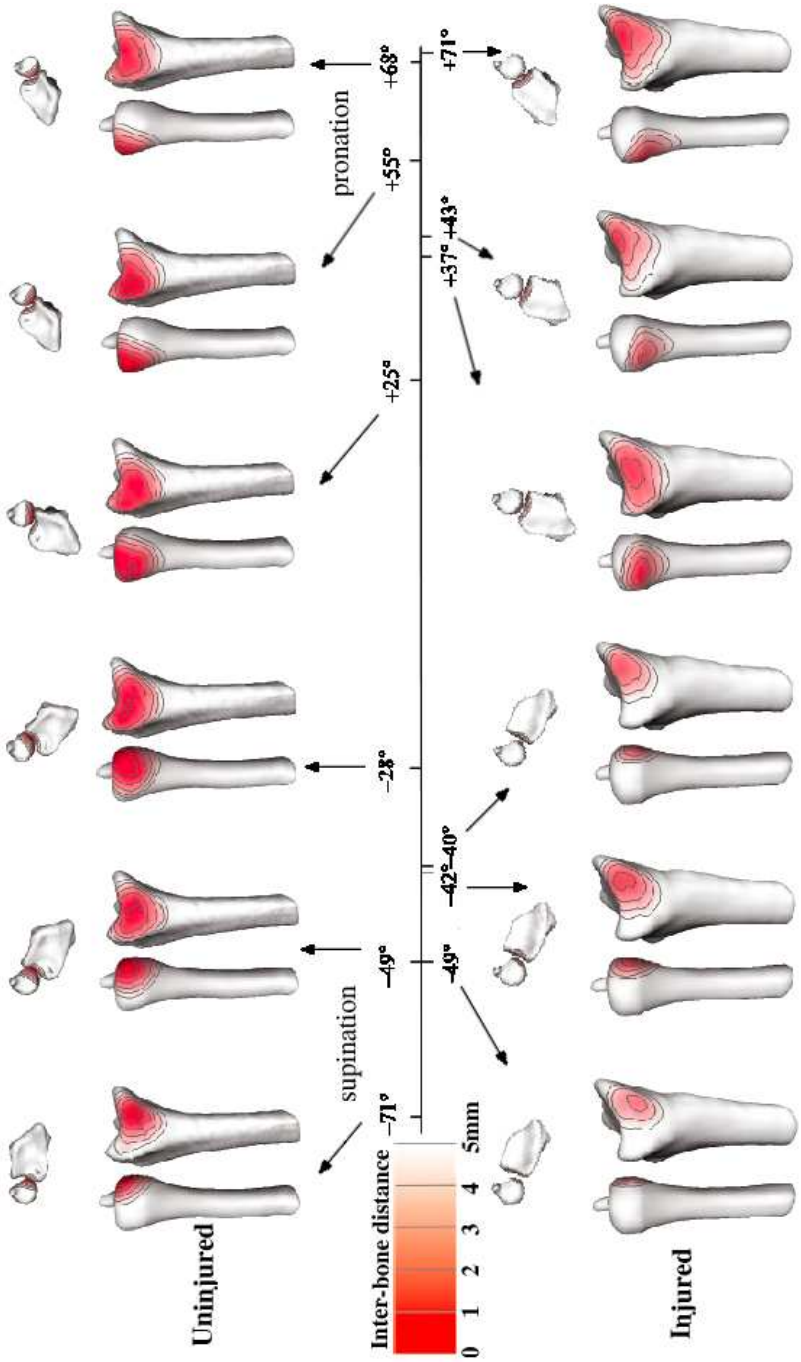

Fig. 11. Proximal and exploded lateral views of an uninjured and an injured radioulnar joint at six rotation positions. Bones are colored according to the distance between them (the closer they are, the more intense the color). Note the shift in the location of the contact areas between the uninjured and the injured forearm.

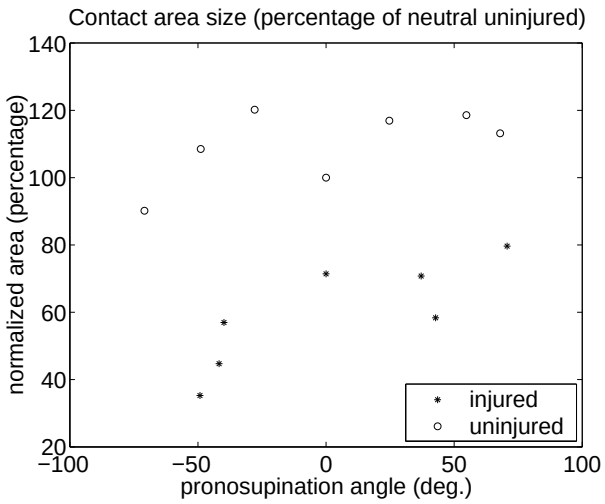

Fig. 12. Size of the ulnar contact area (5 mm threshold) for both the injured and uninjured forearm of the same volunteer. Areas are normalized by the neutral uninjured area. Pronosupination angles are shown on the x-axis. Note the difference in size between the injured and uninjured forearm.

which is larger because it is farther from the center of curvature than the corresponding area on the ulna. Measures based on the ulnar area are reported because they reside in the ulnar coordinate system; the ulnar coordinate system was chosen because it is stationary during pronosupination.

Figure 13 shows the cylindrical coordinates of the ulnar contact area centroid for the uninjured and injured forearm. The increased height coordinate in the injured forearm confirms a shift of the contact area in the proximal direction. The increased distance from the ulnar axis is due to the shift of the contact area on the surface of the ulna to a region of the ulna further from the axis. The angle coordinate plot correlates with the limited range of motion in the injured forearm. The proximal shift in the location of the centroid of the contact area is consistent with the initial diagnosis of radial shortening.

Figure 14 shows distal ligament paths generated for the injured and uninjured forearms of the same volunteer. The lengths generated by our approach are similar to those reported in *in vitro* studies; no *in vivo* information is currently available, to the best of our knowledge. Note that the injured forearm presents ligament-bone impingement for both the dorsal and the palmar ligament. No deflection of the ligaments by the bone is present in the uninjured forearm in any of the rotation positions. Figure 15 shows the dorsal

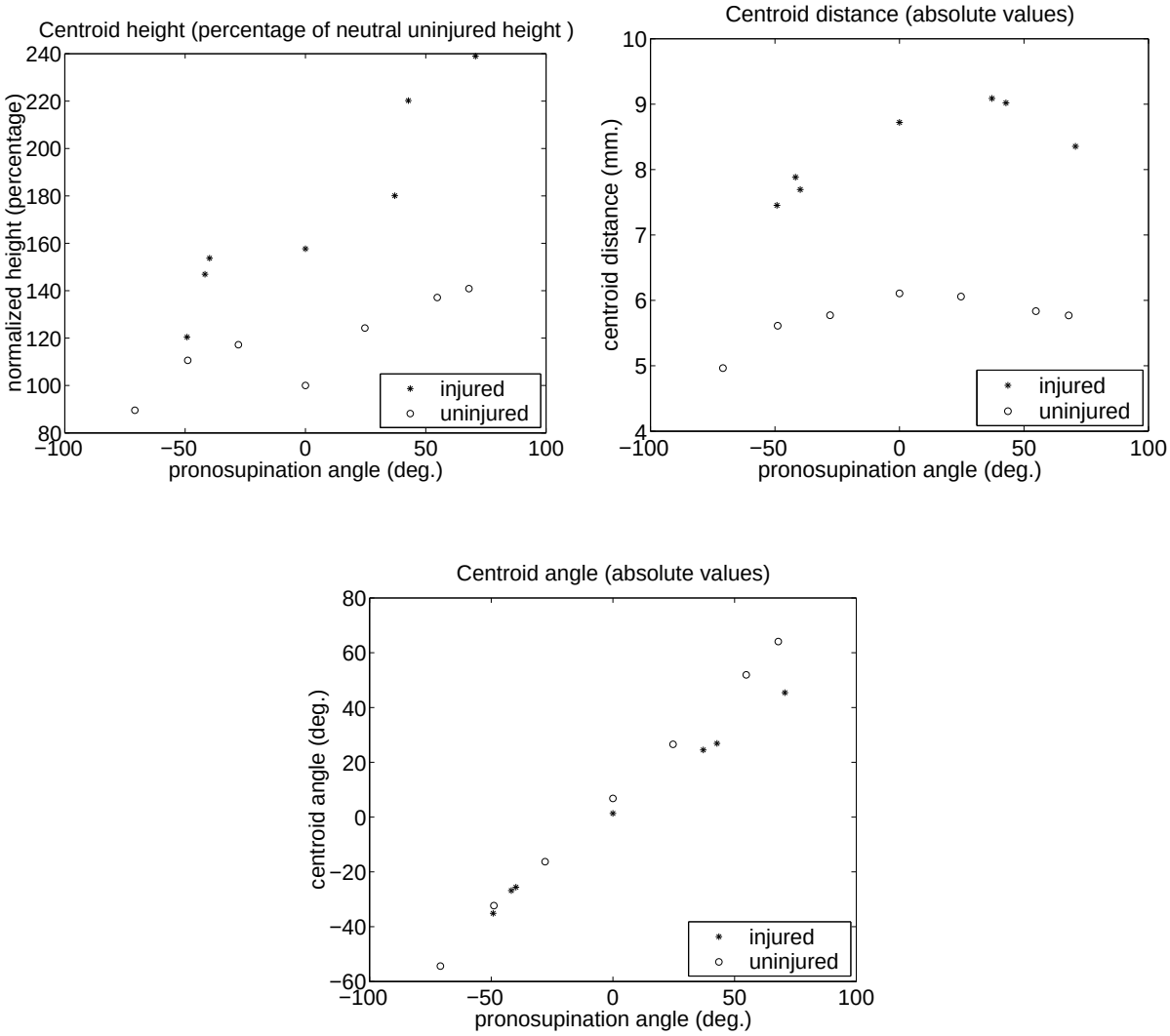

Fig. 13. Cylindrical coordinates (height, distance, and angle) of the ulnar contact area centroid for the injured and uninjured forearms of the volunteer. Heights are normalized by the neutral uninjured height. Pronosupination angles are shown on the x-axis. Note the difference in height and distance between the injured forearm ligament and the uninjured forearm.

radioulnar ligament length and deflection corresponding to the entire pronosupination sequence for the injured forearm. We also show the corresponding lengths and deflection computed for the matching uninjured forearm – note the difference between the two plots. Ligament impingement (measured by the deflection parameter) correlates with ligament path increased length. No ligament deflection is present in the uninjured forearm. The dorsal ligament results generated by displacing the insertion points within the insertion

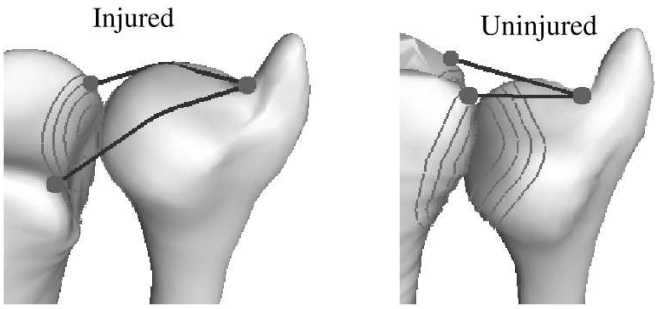

Fig. 14. Distal radioulnar ligament paths in the injured forearm (left) and in the matching uninjured forearm (right) of the same volunteer. Both forearms are in neutral pronosupination (0^o rotation angle). Note the ligament-bone impingement in the injured forearm: both ligaments are deflected by the head of the ulna.

site are plotted in Fig. 17. Note that perturbations in the ligament attachment locations do not affect trends in the comparison measures between the injured and uninjured forearms.

Figure 16 shows plots of the palmar radioulnar ligament length and deflection. Although the palmar ligament length plot shows no difference between the injured and uninjured forearm, we note the impingement (deflection) in the injured forearm, lacking in the uninjured case. The palmar ligament results generated by perturbing the insertion points within the 4 mm diameter insertion sites are plotted in Fig. 18. Note again that perturbations in the ligament attachment locations do not affect trends in the comparison measures between the injured and uninjured forearms.

The change in the dorsal radioulnar ligament length, but not in the palmar radioulnar ligament length, is consistent with the original malunion (radius tilted dorsally). The change in ligament length and the ligament-bone impingement may be one mechanism for the limitation of forearm mobility.

While a single example cannot distinguish between normal anatomical variation and pathological variation, clinical studies on larger sets of patients may establish or refute a correlation between the differences we found here and the injury. Such studies are beyond the scope of this paper.

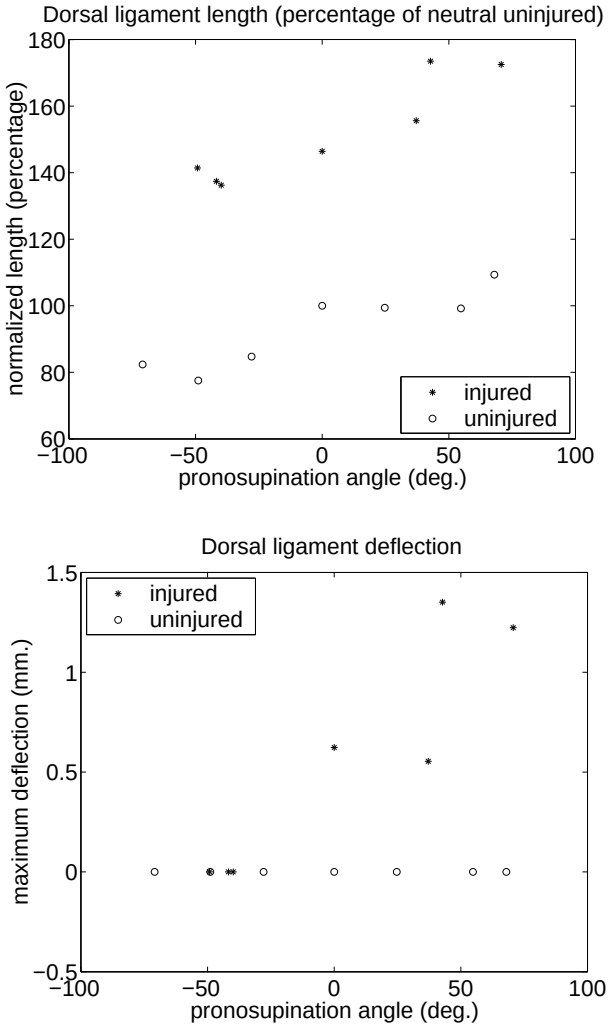

Fig. 15. Length (top) and maximum deflection (bottom) of a dorsal ligament for the injured and uninjured forearms of a volunteer. Lengths are normalized by the neutral uninjured length. Pronosupination angles are shown on the x-axis. Note the increased ligament length in the injured forearm. Note also that no deflection is present in the uninjured forearm.

IV. Related Work

Several approaches to modeling joint surfaces are known; thin-plate splines [18], B-splines [19], [20], and piecewise patches [21] are among them. These methods suffer from problems such as lack of generality, lack of C^2 continuity, and difficulty in enforcing boundary constraints. Our parametrical model for bone surfaces is based on manifolds [22].

Distance fields have been used in robotics [10], [11] and computer graphics [7], [12], [13], [14], [15]. Level sets [16], [17] have been used to generate distance fields and have also

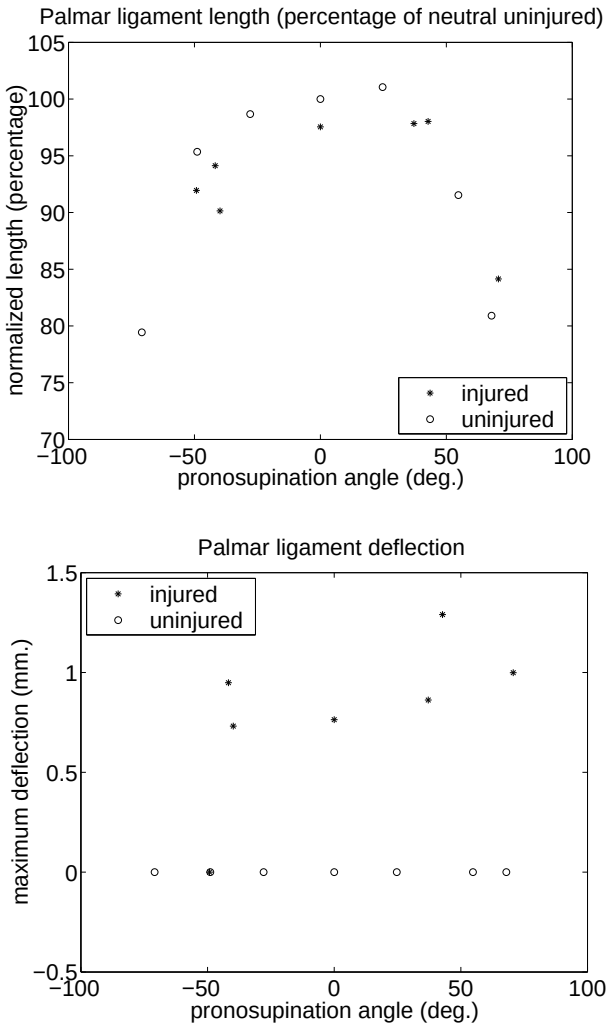

Fig. 16. Length (top) and maximum deflection (bottom) of a palmar ligament for the injured and uninjured forearms of a volunteer. Lengths are normalized by the neutral uninjured length. Pronosupination angles are shown on the x-axis. Note that no deflection is present in the uninjured forearm.

been generated from distance fields.

Searching for shortest paths in spaces with obstacles is a classical problem in robotics. Solutions are based on computational geometry methods [23], [24], [25], [26], differential geometry and hybrid techniques [27], [28], as well as graph search based algorithms [29]. A survey of the substantial literature on the shortest-path problem can be found in [30].

The two scalar data visualization techniques we use, color mapping and isocontouring, are well known scientific visualization techniques [31].

Studies of distal radioulnar ligaments are performed in general on cadaver uninjured

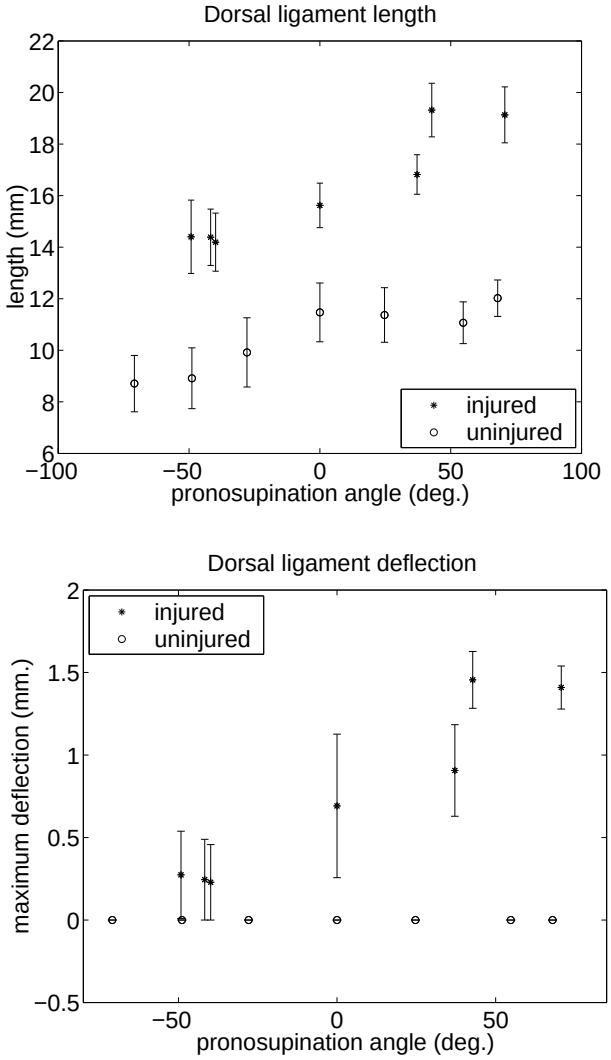

Fig. 17. The effect of insertion point perturbation on the length (top) and maximum deflection (bottom) of a dorsal ligament for the injured and uninjured forearms of a volunteer (mean and standard deviation calculated over 64 measurements).

wrists [32], [33], [34]. A clinical *in vivo* study involving surgery was performed by Kleinman et al. in 1998 [35]. To our knowledge, no *in vivo* noninvasive studies of the distal radioulnar ligaments have been done.

V. Conclusions

We have demonstrated an *in vivo*, noninvasive technique for modeling the length of ligaments and joint contact areas from bone kinematics and surfaces. Our method uses

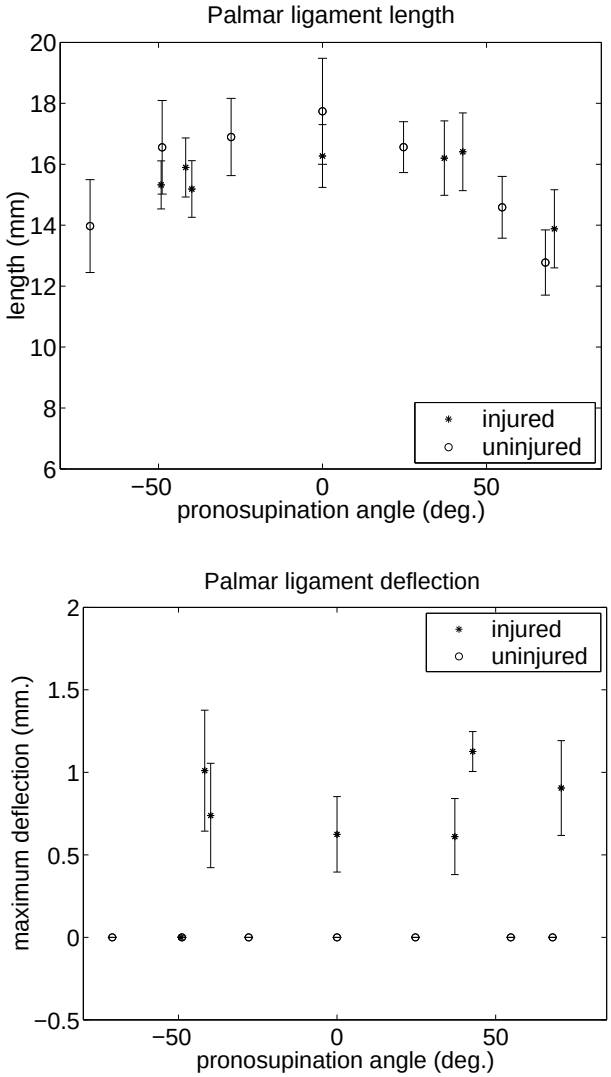

Fig. 18. The effect of insertion point perturbation on the length (top) and maximum deflection (bottom) of a palmar ligament for both the injured and uninjured forearm of a volunteer (mean and standard deviation calculated over 64 measurements).

an implicit model as well as a parametric surface model for each bone. The two types of representation have complementary strengths for different types of calculations. The double representation enables us to model secondary types of information from CT data, such as joint contact areas, intra-joint distances, and plausible ligament paths. Our current ligament model could be enriched by considering other intrinsic and extrinsic ligament factors like tissue composition, muscle forces, and joint compression.

In a demonstration on the DRUJ, our approach highlights subtle modifications, oth-

erwise unnoted, in injured wrist kinematics. Although a previous kinematic study [8] on the same data we analyze in this paper found no significant differences in rigid body kinematics between the injured and uninjured wrist, our method identified potential soft tissue constraints and focal changes in the articulation. The methods presented have the potential to document changes in the joint mechanics that may influence long-term clinical outcome.

Our technique may have applications to the study of wrist disorders such as rheumatoid arthritis, intercarpal ligament tear or attenuation, and carpal-tunnel syndrome. Results suggest that our technique could also be useful in the study of normal anatomy and kinematics of other joints.

Acknowledgments

This work was funded in part by NIH AR44005 and NSF CCR0093238.

References

[1] C. P. Neu, R. D. McGovern, J. J. Crisco, *Kinematic accuracy of three surface registration methods in a three-dimensional wrist bone study*, Journal of Biomechanical Engineering, 122:1–6, 2000.

[2] F. Eckstein, A. Gavazzeni, H. Sittek, M. Haubner, A. Losch, S. Milz, K.H. Englmeier, E. Schulte, R. Putz, and M. Reiser. *Determination of knee joint cartilage thickness using three-dimensional magnetic resonance chondro-crassometry (3d mr-ccm)*, Magn. Reson. Med., 36:256–265, 1996.

[3] V. Feipel, M. Rooze, S. Louryan, and M. Lemort. *Bi- and three-dimensional CT study of carpal bone motion in lateral deviation*, Surg. Radiol. Anat., 14:381–389, 1992.

[4] S.L. Van Sint Jan, G.J. Clapworthy, and M. Rooze. *Visualization of combined motions in human joints*, IEEE Computer Graphics and Applications, November/December: 10–14, 1998.

[5] C. Grimm, J.J. Crisco, and D.H. Laidlaw, *Fitting locally parametric surfaces to 3D point clouds*, ASME Journal of Biomechanical Engineering, 124(1):136–40, 2002.

[6] P. Alexandroff, *Elementary Concepts of Topology*, Dover Publications Inc., 1961.

[7] S.F. Frisken, R.N. Perry, A.P. Rockwood, and T.R. Jones, *Adaptively sampled distance fields: A general representation of shape for computer graphics*, In SIGGRAPH 2000 Conference Proceedings, 2000.

[8] D. Moore, K. Hogan, J. Crisco, E.Akelman, M. DaSilva, and A. Weiss, *3-D In Vivo Kinematics of the Distal Radioulnar Joint in Malunited Distal Radius Fractures*, Journal of Hand Surgery, 27(2):233–242, 2002.

[9] *NAG Fortran Library Routine Document*, http://www.nag.co.uk/numeric/fl/manual/html/e04ucf.html.

[10] R. Kimmel, N. Kiryati and A. Bruckstein, *Multi-valued distance maps for motion planning on surfaces with moving obstacles*, IEEE Trans. on Robotics & Automation,Symposium, 14: 427–436, 1998.

[11] J. Lengyel, M. Reichert, B. Donald and D. Greenberg, *Real-time robot motion planning using rasterizing computer graphics hardware*, Proc. SIGGRAPH 1990:327–335, 1990.

[12] S. Gibson, *Using Distance Maps for smooth surface representation in sampled volumes*, Proc. 1998 IEEE Volume Visualization Symposium:23–30, 1998.

[13] D. Breen, S. Mauch and R. Whitaker, *3D scan conversion of CSG models into distance volumes*, Proc. 1998 IEEE Symposium on Volume Visualization: 7–14, 1998.

[14] B. Payne and A. Toga, *Distance field manipulation of surface models*, IEEE Computer Graphics and Applications:65–71, 1992.

[15] A. Gueziec. *Meshsweeper: Dynamic point-to-polygonal-mesh distance and applications*, IEEE Transactions on Visualization and Computer Graphics, 7(1):47–61, 2001.

[16] S. Osher and J. Sethian, *Fronts propagating with curvature-dependent speed: algorithms based on Hamilton-Jacobi formulation*, J. Computational Physics, 79:12–49, 1988.

[17] J. Sethian, *Level Set Methods: Evolving Interfaces in Geometry, Fluid Mechanics, Computer Vision, and Material Science* , Cambridge University Press, 1996.

[18] S.K. Boyd, J.L. Ronsky, D.D. Lichti, D. Salkauskas, and M.A. Chapman, *Joint surface modeling with thin-plate splines*, Journal of Biomechanical Engineering, 121: 525–532, October 1999.

[19] G.A. Ateshian, *A b-spline least-squares surface fitting method for articular surfaces of diarthrodial joints*, ASME Journal of Biomechanical Engineering, 115:366–373, 1993.

[20] G.A. Ateshian, *Generating trimmed b-spline models of articular cartilage layers from unordered 3d surface data points*, Proc. ASME Bioengineering Conference:217–218, 1995.

[21] P.K. Scherrer and B.M. Hillberry, *Piece-wise mathematical representations of articular surfaces*, Journal of Biomechanics, 12:301–311, 1979.

[22] C. Grimm, J. Hughes, *Modeling Surfaces of Arbitrary Topology using Manifolds*, Computer Graphics, 29(2), July 1995, Proceedings of SIGGRAPH'95

[23] M. Scharir, A. Schorr, *On shortest paths in polyhedral spaces*, SIAM J. Comput.,1(15):193–215, 1986

[24] C.H. Papadimitriou, *An Algorithm for Shortest-Path Motion in Three Dimensions*, Information Processing Letters, 20:259–263, 1985.

[25] K. Clarkson, *Approximation Algorithms for Shortest Path Motion Planning*, Proc. 19th Annual SIGACT Symposium:56–65, 1987.

[26] A. Baltsan, M. Scharir, *On shortest paths between Two Convex Polyhedra*, JACM, 35(2):267–287, 1988.

[27] R. Kimmel, N. Kiryati, *Finding Shortest Paths on Surfaces by Fast Global Approximation and Precise Local Refinement*, Int. Journal of Pattern Recognition and Artificial Intelligence, 10(6):643–656, 1996.

[28] J.M. Beck, R.T. Farouki, J.K. Hinds. *Surface Analysis Methods*, IEEE Computer Graphics and Applications, 6: 18–37, 1986.

[29] N. Kiryati, G. Szekely, *Estimating Shortest Paths and Minimal Distance on Digitized Three Dimensional Surfaces*, Pattern Recognition, 26:1623-1637, 1993.

[30] C.K. Yap, *Algorithmic motion planning*, Advance in Robotics, Volume I, Lawrence Erlbaum Associates, 1985.

[31] K. Martin, W. Schroeder and B. Lorensen, *The Visualization Toolkit: An Object-Oriented Approach to 3D Graphics*, Prentice Hall, 1997.

[32] F. Ekenstam, *Anatomy of the Distal Radioulnar Joint*, Clinical Orthopaedics, 275:14-18, 1992.

[33] R. Acosta, W. Hnat, L.R. Sheker, *Distal radio-ulnar ligament motion during supination and pronation*, The Journal of Hand Surgery (British and European Volume), 18B:502–505, 1993.

[34] F. Schuind, K. An, L. Berglund, R. Rey, W. Cooney, R. Linscheid, E. Chao, *The distal radioulnar ligaments: a biomechanical study*, The Journal of Hand Surgery , 16A(6):1106–1114, 1991.

[35] W. Kleinman, T. Graham, *The distal radioulnar joint capsule: clinical anatomy and role on posttraumatic limitation of forearm rotation*, The Journal of Hand Surgery, 23A(4):588–599, 1998.

List of Figures